



# Multi-mode conversion imaging of the subducted Gorda and Juan de Fuca plates below the North American continent



Benoit Tauzin\*, Thomas Bodin, Eric Debayle, Jean-Philippe Perrillat, Bruno Reynard

Laboratoire de Géologie de Lyon: Terre, Planètes, Environnement, Université de Lyon, Université Lyon 1 and Ecole Normale Supérieure de Lyon, UMR CNRS 5276, F-69622 Villeurbanne, France

## ARTICLE INFO

### Article history:

Received 20 October 2015  
Received in revised form 28 January 2016  
Accepted 31 January 2016  
Available online xxxx  
Editor: P. Shearer

### Keywords:

seismic discontinuities  
receiver functions  
Cascadia subduction zone

## ABSTRACT

Receiver function analysis and seismic tomography show tectonic structures dipping eastward in the mantle below the Cascadia volcanic arc (western US) that have been related to the subduction of the Gorda and Juan de Fuca oceanic micro-plates. Inconsistencies in the dip angle and depth extent of the slab between the two methods undermine the interpretation of the structure and processes at work. Receiver function imaging is biased by multiple reflection phases that interfere with converted phases, and produce spurious discontinuities in images. Here, we correct the interference using a multiple mode conversion imaging technique that efficiently removes artifacts under dipping structures. The method has the advantage of being applicable to large aperture arrays, and can image large-scale structures down to the transition zone. With this approach, the interfaces between the subducting and overriding plates and the oceanic Moho are imaged at shallow depths (<120 km) with a dip angle of  $\sim 20^\circ$ , consistently with former studies. In addition, several important features are imaged with the present method. Faint converters located between 100 and 400 km depth in the mantle wedge, and strong sub-horizontal seismic scatterers near 160 km depth, may highlight dehydration and metasomatism processes in the Cascadia subduction zone. A discontinuity located at  $\sim 15$  km depth in the lithospheric mantle of the subducted plates and associated with a negative impedance contrast is interpreted as the fossil fabric of the plates acquired at the spreading ridges.

© 2016 Elsevier B.V. All rights reserved.

## 1. Introduction

The Cascadia subduction zone is the manifestation of the convergence between the North American plate and the Juan de Fuca and Gorda oceanic micro-plates over the last 6–10 Myr. Seismic imaging of the slab and surrounding mantle beneath this area provides key information to resolve the relationship between continental volcanism and tectonics and the dynamics of the underlying mantle. Despite numerous seismic studies (Xue and Allen, 2007; Burdick et al., 2010; Obrebski et al., 2011; Bostock et al., 2002; Audet et al., 2010; Liu et al., 2012; McCrory et al., 2012), the position of the slab interface at depth and its seismic velocity structure remain controversial. Contrary to older and colder subduction zones such as the Pacific margins, the absence of a well-developed Wadati–Benioff zone in the subducted plate (McCrory et al., 2012) prevents resolving this discrepancy.

In regional tomographic models, the subducted oceanic lithosphere is tracked by eastward dipping fast velocity anomalies (e.g.

Xue and Allen, 2007; Burdick et al., 2010; Obrebski et al., 2011). These studies show a steep subduction ( $\sim 50^\circ$ ) down to the mantle transition zone, whereas most receiver function (RF) analyses (Bostock et al., 2002; Audet et al., 2009, 2010; Liu et al., 2012) show the Juan de Fuca–Gorda plate gently dipping ( $\sim 15^\circ$  to  $30^\circ$ ) at shallow depths (<120 km). Part of this discrepancy results from differences in sensitivity of the two methods. Tomographic models can only constrain the large-scale bulk velocity structure of subducting plates (Grand and van der Hilst, 1997; Káráson and Van Der Hilst, 2000) whereas RF analysis resolves sharp velocity contrasts (Audet et al., 2009; Bostock, 2013) that produce conversions from P to S waves (Langston, 1979).

The reflectivity sequence obtained from classical P-to-S RF imaging in a subduction context is usually contaminated by multiple phases reverberated between the surface and the top of the subducted plate. These free-surface multiples can be accounted for using complex migration schemes that involve a general treatment of seismic scattering (e.g. Bostock and Rondenay, 1999; Bostock et al., 2001). However, these techniques strongly depend on the level of data coverage (Rondenay, 2009), which needs to be dense and uniform. To date, these approaches have only been applied to targeted local arrays of densely spaced stations,

\* Corresponding author.

E-mail address: benoit.tauzin@univ-lyon1.fr (B. Tauzin).

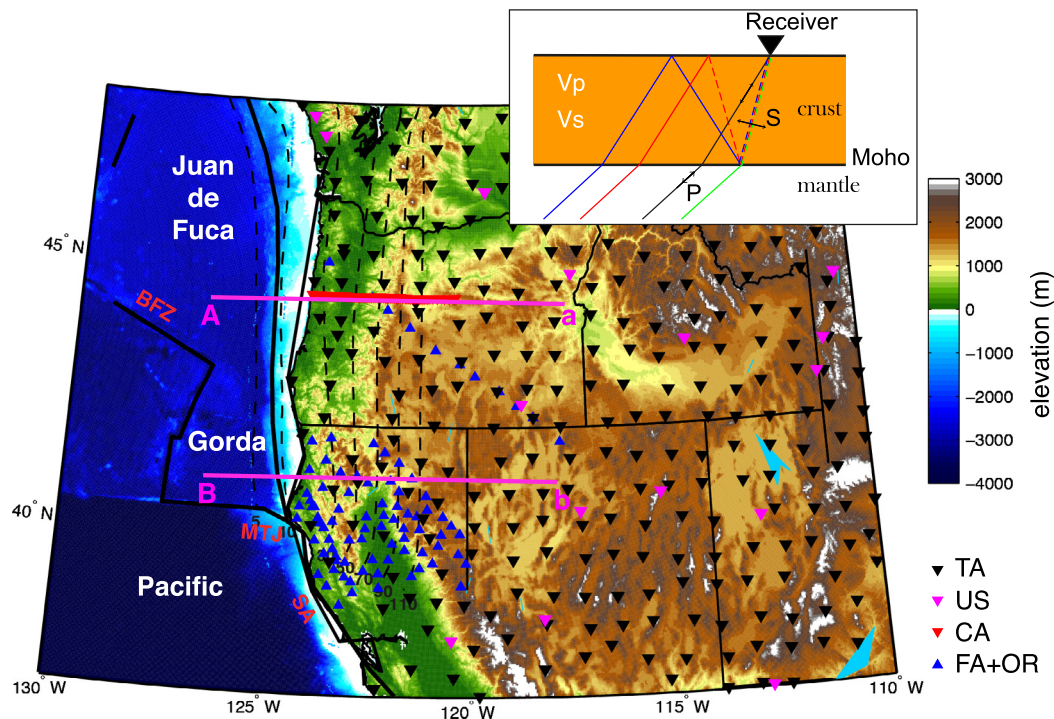


**Fig. 1.** Map of stations used in this study. Two seismic profiles are discussed in the text: A–a makes use of the dense Cascadia 93 linear array of stations (red triangles) in Central Oregon; B–b uses a combination of data from the Transportable Array (black triangles) and the Mendocino experiment (blue triangles) in northern California. Depth contours for the subducted Juan de Fuca Plate (McCroly et al., 2012) are indicated with north–south dashed lines. Acronyms: TA, Transportable Array; FA, FAME Mendocino Experiment; OR, Oregon Telesismic Experiment; CA, Cascadia 93 experiment; US, permanent network. BFZ, Blanco fracture zone; MTJ, Mendocino Triple Junction; SA, San Andreas Fault. Inset: ray geometry of PS waves converted directly at the Moho (green) and reverberated with P–P–S (blue) and P–S–S (red) modes of vibrations within the crust. (For interpretation of the references to color in this figure legend, the reader is referred to the web version of this article.)

e.g. Alaska (Rondenay et al., 2008), Cascadia (Bostock et al., 2002; Abers et al., 2009), Costa Rica and Nicaragua (MacKenzie et al., 2010), western Hellenic (Suckale et al., 2009), and central Mexico (Kim et al., 2012).

In this paper, we use a multiple mode conversion imaging technique that explicitly takes into account the effect of free-surface multiples. It is conceptually simple, easy to implement, and can be applied to larger and sparser arrays to investigate large-scale mantle structures down to 400 km depth. The approach allows us to combine different arrays characterized by various inter-station distances. We complement a previous RF database (61,793 receiver functions) from the US Transportable Array (Tauzin et al., 2013) with two denser arrays of stations: the Cascadia 93 and Mendocino experiments located in central Oregon and northern California (Fig. 1). The wide aperture Transportable Array allows us to depict the western US structure down to the transition zone (TZ) at semi-continental scale. The denser arrays along the A–a and B–b profiles (Fig. 1) increase the number of waveforms by 3490 in central Oregon and by 17,632 in California, providing an up to five times increase in ray coverage of the mantle structure in these regions. These arrays provide a high-resolution image of the subduction system to the west of the North American continent with a better coherence of the slab signature than in the prior study of Tauzin et al. (2013).

This paper is divided into two parts. First, we present the method, establish its robustness on synthetic data for flat and dipping structures, and discuss its advantages compared with other techniques. Second, we reconstruct the reflectivity sequence below Cascadia and re-locate the subduction interface. Our seismic images reveal the existence of new reflectors, located at a depth of about 15 km within the lithospheric mantle of the Gorda and Juan de Fuca plates, and between 100 and 400 km depth in the mantle wedge above the plates. We interpret these signals in the light

of regional tomographic models. The signal at  $\sim 15$  km depth in the lithospheric mantle of the subducted plates is likely associated with the fossil fabric of the plates acquired at the spreading ridges. The deeper converters are tentatively related to pervasive reflectivity from deep slab-dehydration and metasomatism in the mantle wedge of the Cascadia subduction zone.

## 2. Method

A receiver function (RF) is a waveform constructed by deconvolving the vertical component of a teleseismic P wave seismogram from its horizontal component (Langston, 1979). This removes the source and distant path effects in the seismograms and allows us to isolate the effect of the structure below the recording station (Langston, 1979). In this study, we build two datasets by low-pass filtering the broadband seismograms at 1 and 0.2 Hz, respectively. The RFs are then obtained from an iterative time domain deconvolution (Ligorria and Ammon, 1999). The back-projection of the RF waveforms allows us to illuminate the sources of scattering in the subsurface and produce depth seismic sections (see Rondenay, 2009 for a review).

### 2.1. Conventional CCP stacking

#### 2.1.1. The P–S mode

The standard way to interpret receiver functions is by assuming that the energy in the observed signal is due to S waves converted from P waves at discontinuities beneath the recording station. The most common RF imaging method uses direct P-to-S (PS) conversion mode (Langston, 1979) and stacks the data by common conversion points (CCP) assuming conversions at horizontal discontinuities (e.g. Wittlinger et al., 2004). The output of this operation is a reconstructed depth reflectivity sequence, which gives

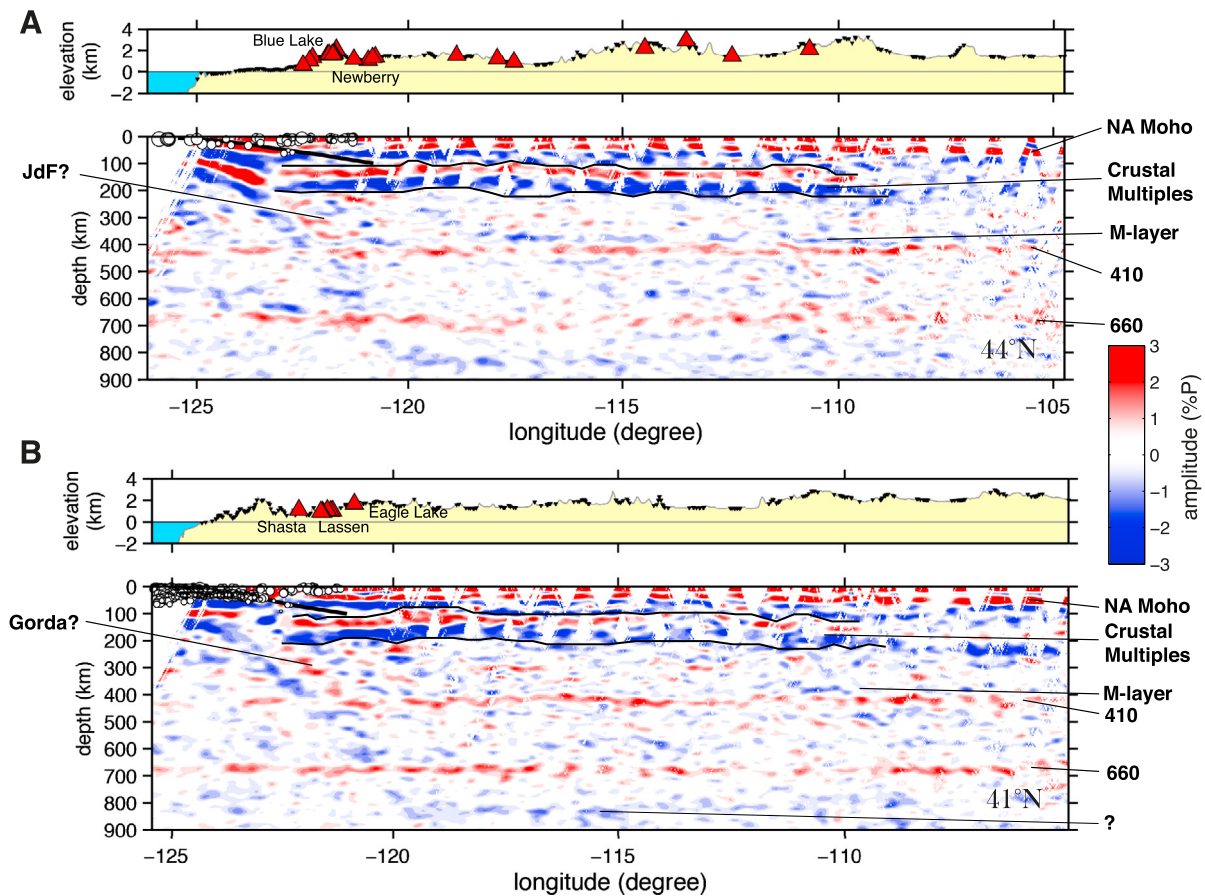


**Fig. 2.** Reflectivity profiles obtained at a large-scale from standard CCP stacking of single-mode PS converted waves at (A) 44.25°N along the A-a profile across central Oregon and (B) 41°N along the B-b profile across northern California. Red/blue areas show respectively positive/negative amplitudes and may be interpreted as increases/decreases in  $v_s$  with increasing depth. In the 100–200 km depth range, the signal of multiple reverberated waves in the crust with P–P–S (red) and P–S–S (blue) modes of vibrations are contoured in black. In the uppermost western part, the dots in the seismic images correspond to a selection of earthquakes above and within the plates from McCrory et al. (2012). Following the seismicity, the depth contour marking the top of the Gorda–Juan de Fuca subducted plate (McCrory et al., 2012) is marked with a thick black line. (For interpretation of the references to color in this figure legend, the reader is referred to the web version of this article.)

a measure of local  $v_s$  jumps as PS seismic scattering is mainly sensitive to variations in  $v_s$ . In Fig. 2, we present two seismic profiles obtained from standard CCP stacking, and corresponding to the A–a and B–b profiles in Fig. 1. For the time-to-depth conversion, we used the IASP91 (Kennett and Engdahl, 1991) one-dimensional velocity model. The model discretization uses cells with 1 km vertical and 2 km lateral dimensions, and the level of smoothing is identical to that used in Tauzin et al. (2013). Remarkable features are the positive amplitude signals (red) associated with the PS conversions at the Moho discontinuity near 35 km depth, and at the 410 and 660 discontinuities in the TZ. An intermittent sub-horizontal negative signal (blue) is associated with a low- $v_s$  layer (M-layer) atop the 410 discontinuity (Song et al., 2004; Schmandt et al., 2011; Tauzin et al., 2010, 2013). It is mostly visible below central Oregon (Fig. 2A). This signal marks the top of a layer with a sharp reduction of  $v_s$  (2–3%). Another negative signal (blue) is located near ~800 km depth in the lower mantle, but with an undetermined origin.

Seismic phases reverberated multiple times in layers over-lying major interfaces (see inset in Fig. 1) are also recorded on the RFs. These back-scattered waves, comprising P–P–S (PPS) and P–S–S or S–P–S (PSS) modes of vibrations, are called multiples or reverberations. They are generally considered as noise or artifacts as they prevent from interpreting the structure below these interfaces. In Fig. 2, the reverberations within the crust are contoured with black lines. They overwhelm and obscure the signal associated with the structure between 100 and 200 km depths. The

PPS and PSS phases show up as a succession of positive (red) and negative (blue) arrivals when they reverberate at the top of a positive velocity contrast (in red), such as the Moho. As shown in the next section, the dipping structures in the west crossing the transition zone are also likely artifacts resulting from these PPS and PSS modes of conversions.

### 2.1.2. The case of dipping structures

Below the Cascadia volcanic arc, an eastward dipping signal reaches the lower mantle near 120°W (Fig. 2). Tauzin et al. (2013) observed this dipping signal from 39° to 48°N and suggested that it is associated with the signature of the Gorda micro-plate to the south, and Juan de Fuca micro-plate to the north (Fig. 1). This steep signal was not observed in previous RF studies (Bostock et al., 2002; Audet et al., 2010), active source seismic profiling (e.g., refraction, wide-angle reflection) or seismicity studies (McCrory et al., 2012). These studies rather suggest that the Gorda and Juan de Fuca plates reach ~100 km depth near 121°W, as shown in Fig. 2 by the depth contours of the plates from McCrory et al. (2012).

The results of synthetic tests shown in Fig. 3 confirm that spurious signals associated with strong multiple reverberations, such as in Fig. 2, can easily be mistaken with a steeply dipping layer. We calculated seismograms for the same acquisition geometry as in northern California from a ray-based algorithm of Frederiksen and Bostock (2000), and processed them in the same manner as the actual data. The velocity models used to generate the synthetics are given in Table 1. In model-1, we used 4 homogeneous

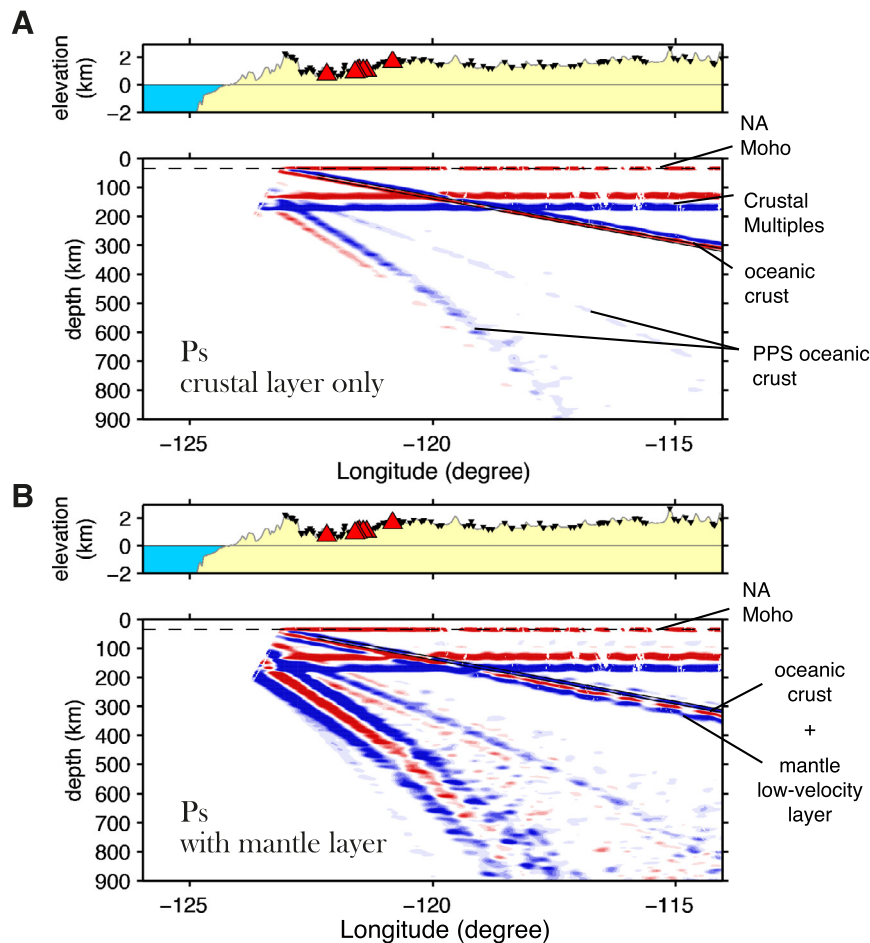


**Fig. 3.** Synthetic signals obtained from the single-mode PS CCP stacking for the models of Table 1. (A) Model-1: a model including a low-velocity oceanic crust dipping at  $20^\circ$  in the mantle. (B) Model-2: a model including a low velocity crustal layer and a sharp decrease of velocities 15 km below the oceanic Moho in the subducted lithospheric mantle. The second model better explains the observations of amplitudes of reverberated waves below central Oregon and California in Fig. 2.

**Table 1**

Velocities used for the synthetic tests of Figs. 3 and 5. The  $v_p$  models are scaled with  $v_p \sim 1.8v_s$  (taken from IASP91). The density has little effect on conversion amplitudes of PS converted waves. It is fixed at  $2600 \text{ kg/m}^3$  in the continental crust,  $3500 \text{ kg/m}^3$  in the oceanic crust and the mantle.

Layers	Model-1 $v_s$ (km/s)	Model-2 $v_s$ (km/s)
Continental crust	3.7	3.7
Continental mantle	4.5	4.5
Oceanic crust	3.4	3.4
Normal oceanic mantle	4.5	4.5
Lower- $v_s$ oceanic mantle	-	3.4

layers including a continental crust, a continental lithosphere, and a low-velocity oceanic crust overlying an oceanic lithospheric mantle. The continental velocities are taken from a typical continental lithosphere. The velocity in the oceanic crust is fixed to simulate the velocity jump at its top, and the dip angle of the crust is set to  $20^\circ$ , close to what is inferred from RF studies below Cascadia (Bostock et al., 2002; Audet et al., 2009; Bostock, 2013). Model-2 is similar to model-1 except that a sharp reduction of velocities is set in the oceanic lithospheric mantle 15 km below the oceanic Moho.

In the synthetic test of Fig. 3A, the multiples of the oceanic crust dip steeply below the Cascadia volcanic arc to reach 500 km depth near  $120^\circ\text{W}$  longitude, similar to what is observed with real data in Fig. 2. This demonstrates that the steep signals observed in the western US could be due to multiples rather than direct P-to-S

conversions at the slab interfaces. We show with the synthetic test from model-2 in Fig. 3B that the sequence of multiples observed in real data is better reproduced when including a sharp reduction of velocities in the lithospheric mantle of the oceanic plate.

Thus the interpretation of standard single mode CCP imaging must be done with caution, especially in the context of subduction zones (Song et al., 2004; Schmandt et al., 2011; Tauzin et al., 2013). The effect of reverberations is particularly critical for the analysis of seismic discontinuities below the plate structure. Synthetic tests in Fig. 3 highlight the probable interference of the strong sequence of multiples below the slab with the transition zone structure, preventing for instance the precise characterization of the low-velocity layer atop the 410 for longitudes west of  $120^\circ\text{W}$  (Song et al., 2004; Schmandt et al., 2011; Tauzin et al., 2013).

## 2.2. Multi-mode CCP stacking

We used a multiple mode conversion imaging technique (Hetényi, 2007; Nábělek et al., 2009) to explicitly take into account the effect of free-surface multiples, reconstruct the correct reflectivity sequence below Cascadia, and re-locate the subduction interface. In addition to the PS mode of conversion, we back-project the energy as if it was produced by the back-scattered PPS and PPS modes (see inset in Fig. 1). Ray-tracing through the IASP91 velocity model (Kennett and Engdahl, 1991) gives the theoretical travel times of these different phases for converters/reflectors at any depth in the model. We back-project the amplitudes measured

at these times on the RFs to the theoretical location of scatterers, either as forward (i.e. direct conversion) or backward scattering (i.e. multiples). Each individual mode is thus handled separately, and produces a separate image.

Due to an increase of velocity with depth in the reference model, the time-to-depth conversion warps the late signal (i.e. mainly the multiples) more than the earlier signal in the RFs. To take into account this stretching effect and turn the forward and back-scattered images to similar wavelengths, the data are filtered with different low-pass corner frequencies (Hetényi, 2007; Audet et al., 2009), at 1 Hz for PS, and 0.2 Hz for PPS and PSS.

The final image is constructed by stacking the three images obtained from the different modes. However, each individual image contains artifacts from other modes, i.e. parallel echoes of the real structure (Rondenay, 2009). For example, PS conversions are mapped at shallower depths in the image constructed with the PPS mode, etc. (see section 2.2.1 below). To remove these artifacts in the final image, we proceed to a phase-weighted stack, where only signals that are coherent from one mode to another are stacked (Schimmel and Paulssen, 1997). Below we illustrate and test the method in two different synthetic settings, before applying it to our data set in western US.

### 2.2.1. The case of a flat stratification

The multi-mode CCP stacking is first illustrated (Fig. 4) on synthetic receiver functions (RFs) computed for the Transportable Array geometry in the IASP91 model (Kennett and Engdahl, 1991). For every source–receiver pair in our database, full-waveform synthetic seismograms have been computed using a reflectivity algorithm (Fuchs and Müller, 1971). The source parameters are from the global CMT catalogue (<http://www.globalcmt.org/>). Receiver functions are constructed in the same way as the real data. The 2D profiles shown in Fig. 4 are obtained along the B–b profile across northern California.

The classical CCP stacking for the PS mode is shown in Fig. 4A, where reverberations between the surface and the two crustal interfaces (PPS, PSS) are clearly visible in the 80–180 km depth range. When stacking the 0.2 Hz PPS phases (Fig. 4B), the positive PPS crustal multiple is re-positioned (in red) at the depth of the Moho discontinuity (35 km depth). The negative PSS crustal multiple (in blue) is also present, underlying the Moho, and representing a fictitious interface in the PPS imaging (Fig. 4B). In Fig. 4C, for the purpose of comparison with the PS and PPS modes, we reverse the polarity of the stacked image because the PSS phase has a negative polarity. The result is similar to Figs. 4A–B, except that the now negative PPS multiple locates atop the Moho signal obtained from the PSS phase. In Fig. 4D, the subsequent stacking of the PS, PPS, and reversed-polarity PSS images, enhances the coherent signal in all three images. It partly removes the signal of crustal reverberations, allows the recovery of a strong Moho interface, and of a faint crustal Conrad discontinuity at 20 km depth.

However, in Fig. 4D, the mix of direct conversions and multiple reverberations gives a sequence of fictitious converters with alternating polarities at the vicinity of the Moho. In addition, other seismic arrivals contribute to the stacked images: the PS conversion at the 410-km discontinuity is mapped near 200 km in the PPS (Fig. 4B) and near 90 km in the PSS (Fig. 4C) images. The conversion at the 660-km discontinuity is also mapped near 150 km depth in the PSS image (Fig. 4C). The crude linear stacking of the three images succeeds partially at removing these fictitious interfaces, but energy from these out of phase modes remains. To remove the problems arising from this cross-mode contamination, we build Fig. 4E from a phase-weighted stack (Schimmel and Paulssen, 1997). This operation efficiently filters out the signals that are not coherent between different modes: it removes the effects of TZ discontinuities in the upper mantle as well as the

sequence of alternating polarity converters in the vicinity of the Moho over the whole profile (Fig. 4E). The only remaining converters are the Moho and Conrad discontinuity in the crust.

### 2.2.2. The case of a dipping stratification

CCP imaging implements ray tracing within Earth models with the assumption of horizontal discontinuities. If dipping interfaces are not taken into account, it can result in a number of artifacts like distortion, incorrect recovery of the interface dip angle, and in some cases amplitude reversal (Frederiksen and Bostock, 2000; Lucente et al., 2005). A recent study on RF migration (Cheng et al., 2016) shows that past 30° of dip angle, single mode CCP is unable to recover a dipping layer.

In Fig. 5, the efficiency of our multi-mode CCP stacking is tested on synthetic data computed for dipping structures. The seismograms are calculated using the ray-based algorithm of Frederiksen and Bostock (2000) with the Model-1 of Table 1, and varying the dip angle of the oceanic crust with values of 5°, 10°, 20°, and 40°. The acquisition geometry is associated with the stations of the Transportable Array and the Mendocino experiment along the B–b profile. The model used for multi-mode CCP stacking is IASP91 (Kennett and Engdahl, 1991), different from the Model-1 used for computing the synthetic RFs.

When the dip is lower than 20° (Figs. 5A, 5B), our multi-mode CCP procedure is efficient at recovering the low-velocity layer. In this case, discontinuities are imaged with the correct dip angle, and with little residual energy left from cross-mode contamination. In the case of steeper structures (Figs. 5C, 5D), ray geometries and travel times computed in the 1D reference model are misestimated, and hence the different modes do not stack coherently anymore. In this case, real seismic discontinuities in the migrated profile cannot be enhanced with the phase weighted stack, which significantly lowers the signal to noise ratio of CCP images. Another well known effect of dipping interface is that they generate a  $2\pi$  periodicity in the move-out of converted arrivals as a function of back-azimuth (Frederiksen and Bostock, 2000; Lucente et al., 2005). As a result, receiver functions measured at different back-azimuths do not stack coherently, thus producing outlined artifacts in the depths sections of Figs. 5C and 5D. Finally, since the 1D reference model used for time-to-depth conversion, IASP91, differs from the one used in computing the RFs (Table 1), the slab-top and slab-bottom arrivals appear to be diverging in Fig. 5C. Imaging a dipping Moho with an angle as high as 40° remains however possible (Fig. 5D).

### 2.3. Application to the western US data

The application of the multi-mode CCP stacking to US data along the B–b profile is shown in Fig. 6. Compared to Fig. 2B, the use of 1 Hz PS conversions (Fig. 6A) improves the vertical resolution. The North American continental Moho is well imaged throughout the whole profile. The Gorda Moho is also visible (red) in the uppermost western part, although it is faint below 40 km depth. When stacking the 0.2 Hz PPS phases (Fig. 6B), the positive PPS crustal multiples of the Moho of the North American and Gorda plates are re-positioned (in red) at the depth of the Moho discontinuity, near 35 km for the continental Moho, and dipping from 20 to ~120 km depths for the oceanic plate. As emphasized on the synthetic test of Fig. 4B, the PSS crustal multiple contributes to the negative signal (in blue) under the Moho of both plates (Fig. 6B). The result of stacking and reversing the polarity of the PSS phase (Fig. 6C) gives similar results to Fig. 6B, showing the flat continental and dipping oceanic Moho, except that the negative PPS multiple (in blue) contributes to the signal atop the oceanic

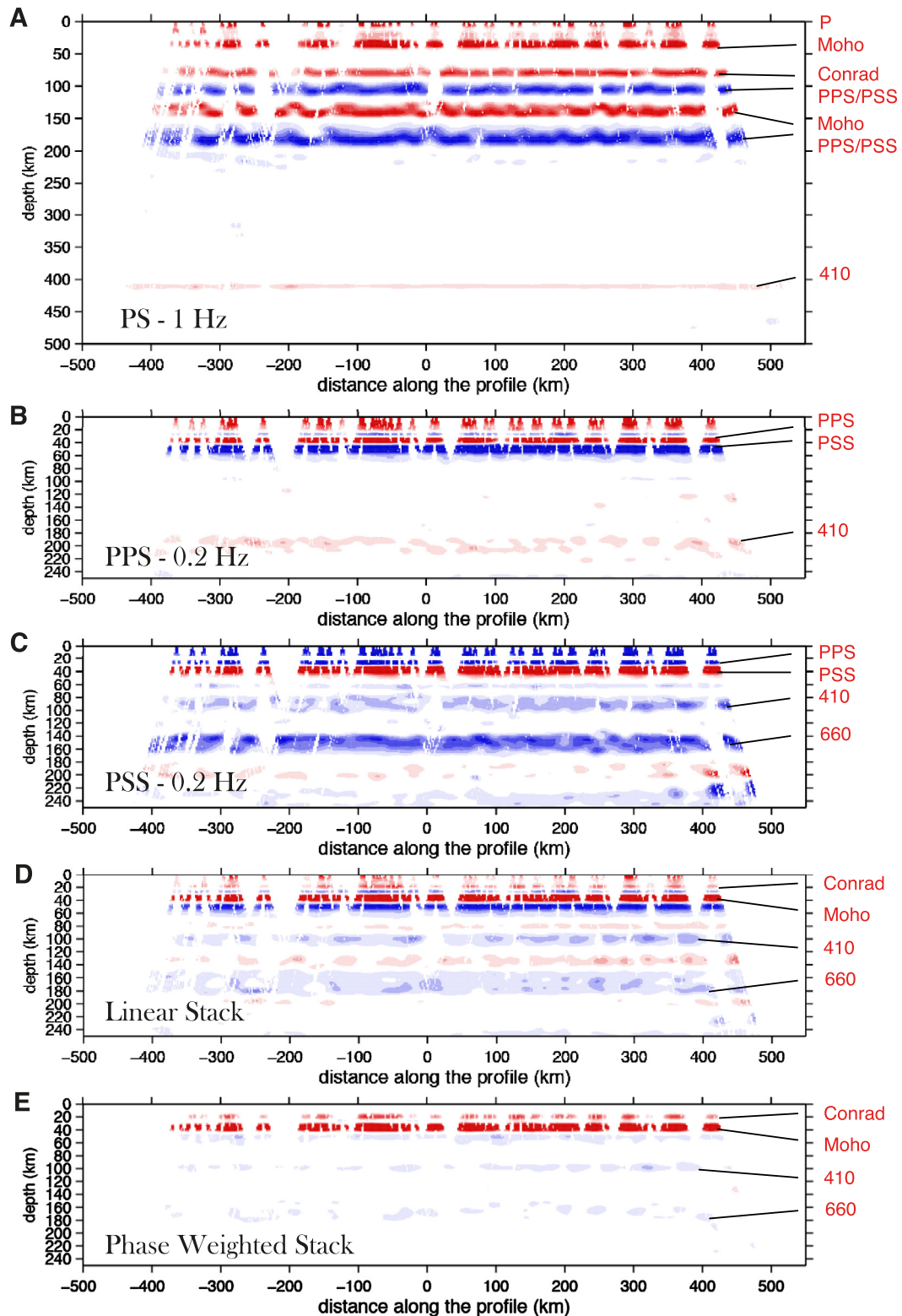


**Fig. 4.** Multi-mode common conversion point (CCP) stacking and the phase-weighted stack (Schimmel and Paulssen, 1997) applied on synthetic receiver functions for the IASP91 velocity structure (Kennett and Engdahl, 1991) and the Transportable Array geometry of acquisition. The crustal structure in IASP91 has two interfaces, the Conrad discontinuity at 20 km depth and the Moho at 35 km depth. (A) Classical CCP stacking for the PS scattering mode. (B) Stacking for the PPS scattering mode. (C) Stacking for the PSS scattering mode. The polarity has been reversed. (D) A crude linear stacking of the PS, PPS, and  $-PSS$  modes shows fictitious interfaces within and below the crust. (E) The phase-weighted stack allows retrieving efficiently the Conrad and Moho discontinuities and removing these artifacts. (For interpretation of the references to color in this figure, the reader is referred to the web version of this article.)

Moho. In Fig. 6D, the subsequent phase-weighted stack of the PS, PPS, and reversed-polarity PSS images enhances the coherent signal in all three images, and allows building a clearer image of the Gorda plate subducting below northern California.

In the case of central Oregon, we show in Fig. 7 that our multimode CCP image is similar to the image obtained with a 2D generalized radon transform (GRT, Bostock et al., 2002), i.e. a more complex method involving the inversion of the full elastic scat-

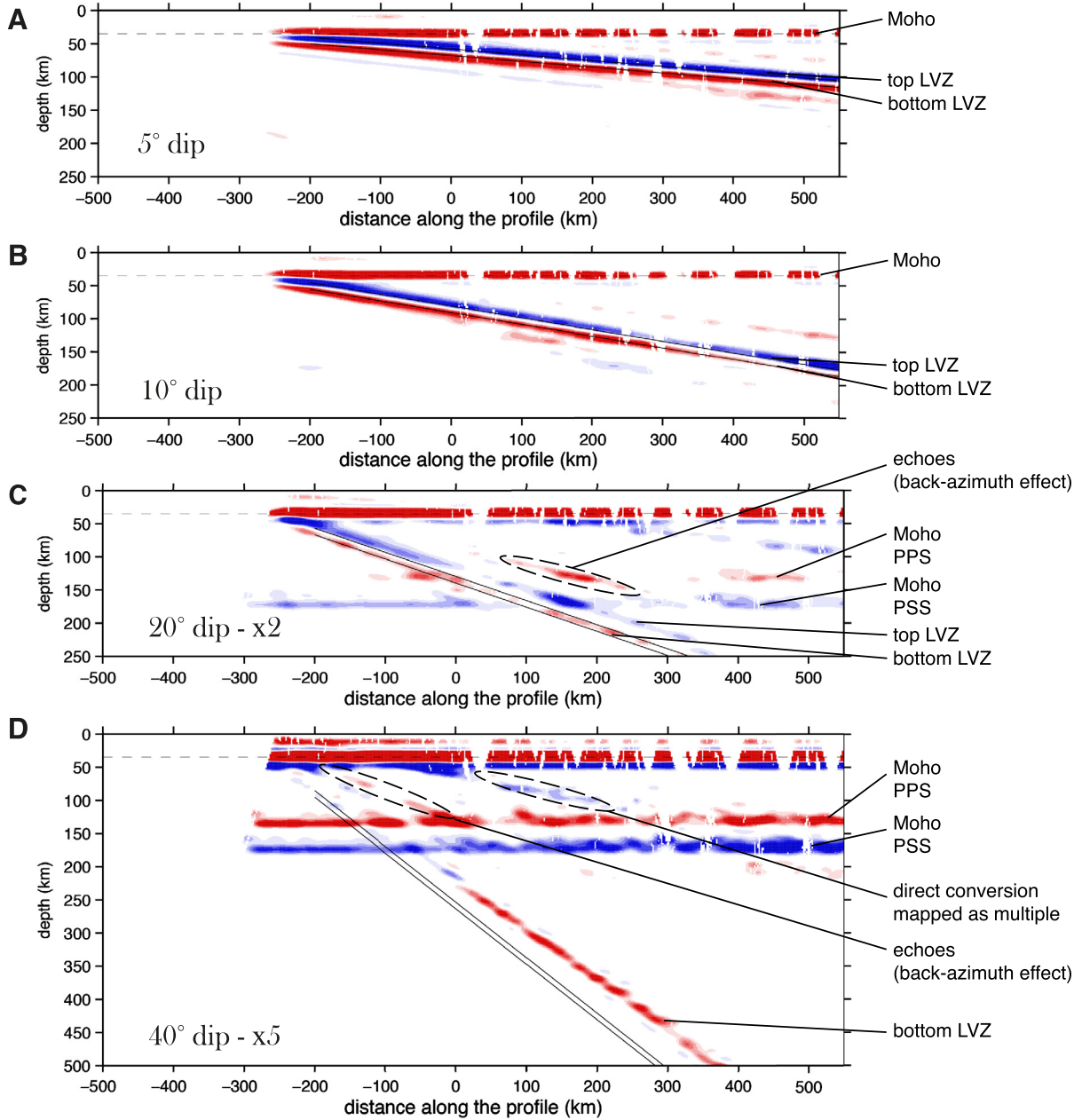


**Fig. 5.** A synthetic test for the recovery of 5°, 10°, 20°, and 40° dipping low-velocity crustal layers below northern California (A–D). With this geometry of acquisition, multi-mode CCP stacking is efficient to recover a dipping structure. However, the error on the signal amplitude (amplified with a factor 2 and 5 in C and D) and the recovery of the dip angle increases with the angle of the input structure. A test with a 50° dip angle gives a similar result as in case (D).

tered wavefield. The two methods produce equivalent results, with interfaces located in the same places. The North American Moho of [Bostock et al. \(2002\)](#) matches ours perfectly. We map the low-velocity oceanic crust at a slightly shallower depth, possibly due to a difference in the reference velocity model used for time-to-depth conversion. However, an advantage of our method is the ability to jointly interpret datasets from arrays of different sizes and densities, and with different resolving power. While the GRT is limited to small dense arrays and only maps structure down to 120 km depth in [Fig. 7](#), multimode CCP imaging allows us to combine small arrays with USArray data, and map features down to the transition zone. It also remains computationally tractable and cheap (the time of computation barely exceeds one minute on a typical desktop computer).

### 3. Results and discussion

The final reflectivity profiles for the Cascadia subduction zone below central Oregon and northern California are shown in [Figs. 8A and 8B](#). Multi-mode CCP imaging gives a simple and shallow image of the subducted plate, marking the Moho of the Gorda and Juan de Fuca plates as continuous converters in red down to ~120 km depth, and in agreement with the pattern of seismicity and the slab contours estimated by [McCrory et al. \(2012\)](#), [Bostock et al. \(2002\)](#) ([Fig. 7](#)), and [Audet et al. \(2010\)](#).

In the oceanic plate ([Fig. 8](#)) extending from ~50 km to ~120 km depth, we observe a negative signal (blue) marking a sharp reduction of velocities in the lithospheric mantle of the subducted plates. It is located at ~17 and 21 km below the oceanic

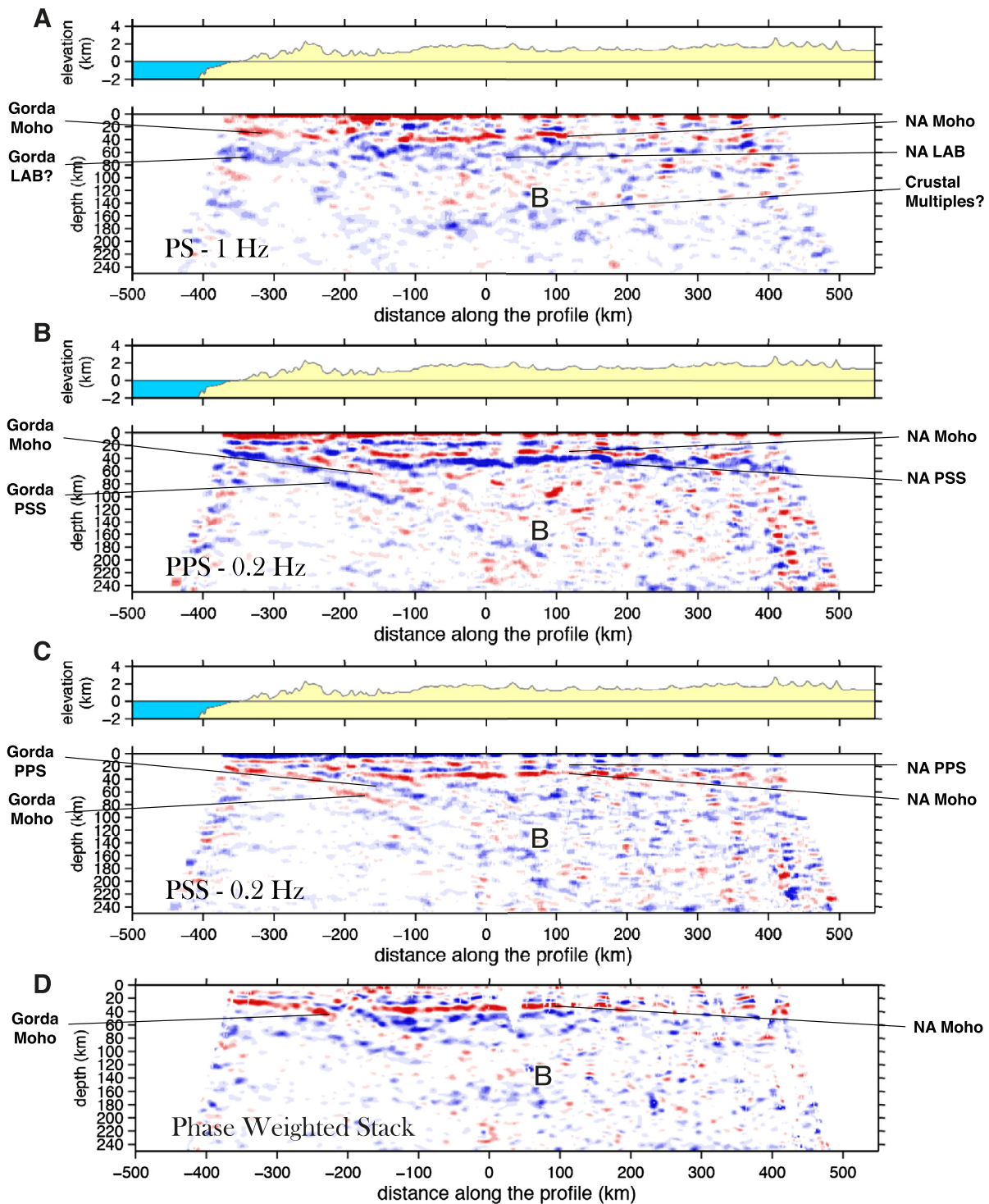


**Fig. 6.** Construction of the composite image for the subduction zone below northern California. (A) Stacking for the PS mode. (B) Stacking for the PPS mode. (C) Stacking for the PSS mode for which we display the opposite of the observed amplitudes. (D) Composite image built by phase-weighted stack of the PS, PPS and reversed-polarity PSS images. (For interpretation of the references to color in this figure, the reader is referred to the web version of this article.)

Moho in central Oregon and in northern California, respectively. The synthetics in Figs. 5 show that for the observed dip angles near  $20^\circ$ , dipping interfaces are properly recovered by multi-mode CCP stacking. In addition, we show in Fig. 3 that the sequence of multiple phases observed in Fig. 2 (negative-under-positive-under-negative amplitudes) is better reproduced when including a sharp reduction of velocities in the lithospheric mantle (Model-2 of Table 1). This converter thus can reliably be interpreted as a  $v_s$  reduction.

The origin of this reduction of velocities in the subducted lithospheric mantle is uncertain. A first hypothesis associates this converter with the thermally controlled lithosphere–asthenosphere boundary (LAB) of the oceanic plates. The thermal boundary layer thickness would vary from 25 to 55 km for a 5–10 Myr old lithosphere according to the half-space cooling model. Taking into account a  $\sim 7$  km thick crustal layer, this is at the lower limit but not incompatible with the thickness that we observe from the oceanic Moho (17–21 km). In oceanic areas, surface-wave seismic

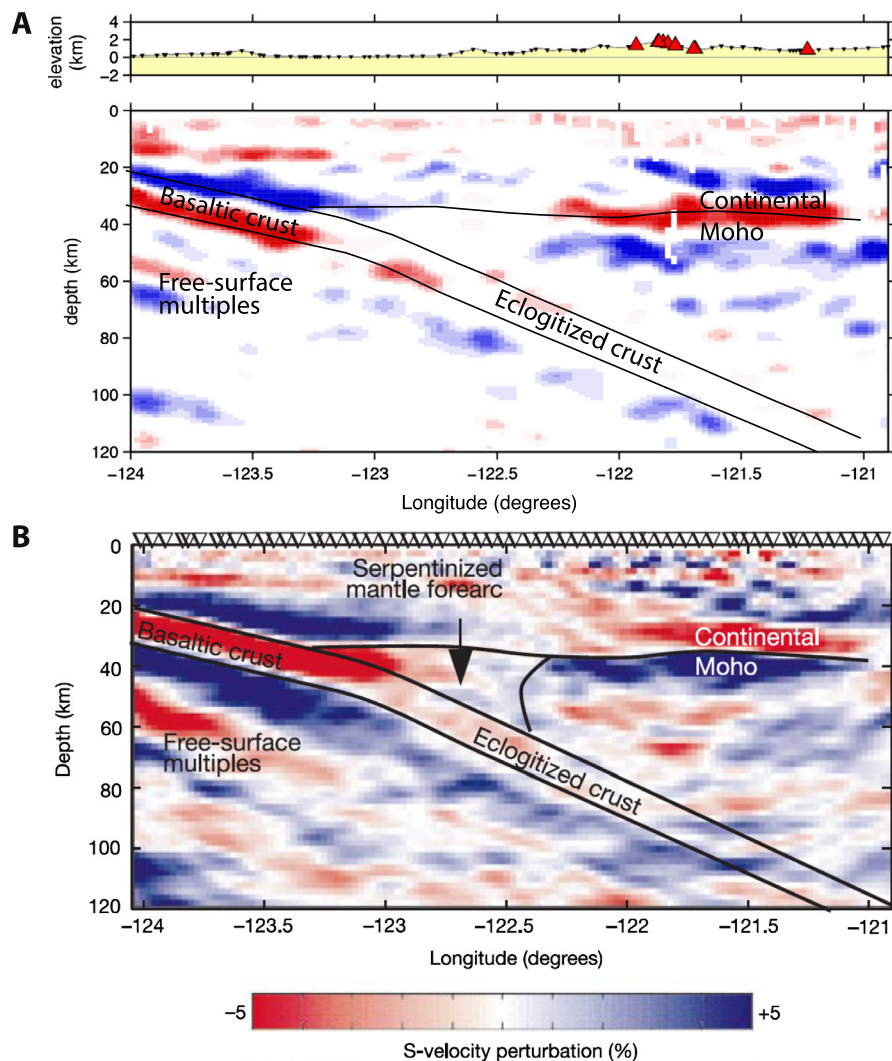


**Fig. 7.** Seismic profiles obtained from the Cascadia 93 experiment at  $\sim 44.25^\circ\text{N}$  across central Oregon. (A) Result of our CCP stacking algorithm using the PS, PPS and PSS scattering modes. We superimpose the interpretation of [Bostock et al. \(2002\)](#), with the location of their interfaces. (B) The result from the 2D generalized transform migration from [Bostock et al. \(2002\)](#), using also the three scattering modes, but adding a supplementary step of inversion for perturbations of  $v_s$  relative to a reference model.

tomography is commonly used to describe the thermal structure of oceanic plates (e.g. [Debayle and Ricard, 2012](#)). These studies use a kink in the inverted velocity profiles as a proxy for the bottom of the lithosphere. In [Fig. 9](#), we superimpose our images on cross-sections through DNA10, a regional shear-wave tomographic model ([Obrebski et al., 2011](#)). This model includes surface and body waves and can be used to estimate the thickness of the lithosphere. In both sections, the negative converter is located in the uppermost part of the fast slab anomaly ([Fig. 9](#)), suggesting that this converter is not the thermally controlled LAB.

A second explanation involves volatiles trapped within the subducted plate. The crust and the upper mantle portion of the subducted plate are able to carry mineral-bound  $\text{H}_2\text{O}$  in the form of serpentine and possibly chlorite to depths greater than 65 km ([Hacker et al., 2003](#)). The top of a low-velocity hydrated serpentine-chlorite layer could mark the RF images with a negative signal in the subducted lithospheric mantle. The chlorite phase is predicted to break down when the slab top reaches  $\sim 80$ – $90$  km depth ([Hacker et al., 2003](#); [Walowski et al., 2015](#)), which is directly beneath the volcanic arc. Interestingly, the negative signal in [Fig. 8](#) disappears near 110 km depth past the volcanic arc. However, from the few known mechanisms providing water to the oceanic lithospheric mantle (see e.g. [Faccenda et al., 2009](#); [Faccenda, 2014](#)), none of them appear efficient enough to trap

large amounts of water at depths greater than 15 km below the oceanic Moho. [Nedimović et al. \(2009\)](#) showed from multichannel seismic data that the depth extent of fault structures in the seafloor offshore of the Cascadia margin is likely limited to Moho depths, a configuration that would prevent deep hydration of the lithospheric mantle. From the current constraints, a reduction of velocities due to deep hydration of the subducted lithospheric mantle thus appears unlikely ([Reynard et al., 2010](#)).

A third possibility involves frozen anisotropy in the sub-crustal oceanic lithosphere inherited from the alignment of olivine minerals in the spreading direction of the plate near the ridge ([Beghein et al., 2014](#); [Song and Kim, 2012](#)). [Shinohara et al. \(2008\)](#) reported such a shallow low velocity and anisotropic zone at  $\sim 30$  km depth in the  $\sim 80$  km thick lithosphere of the  $\sim 50$  Myr old Pacific plate. The detection of a negative discontinuity arising from anisotropy is dependent on the relative orientations of the overlying and underlying fabrics, the strength of the anisotropy in each layer, and the azimuthal sampling provided by the source–receiver paths ([Reynard et al., 2010](#)). [Audet \(2013\)](#) demonstrated that a lithospheric mantle interface observed in the subducted plate at the North of Cascadia and beneath several other subduction zones in the world (Nankai, Mexico, Costa Rica) is consistent with the fossil fabric generated at the spreading ridges. Several methods have been proposed to constrain the seismic anisotropy from RFs. A first

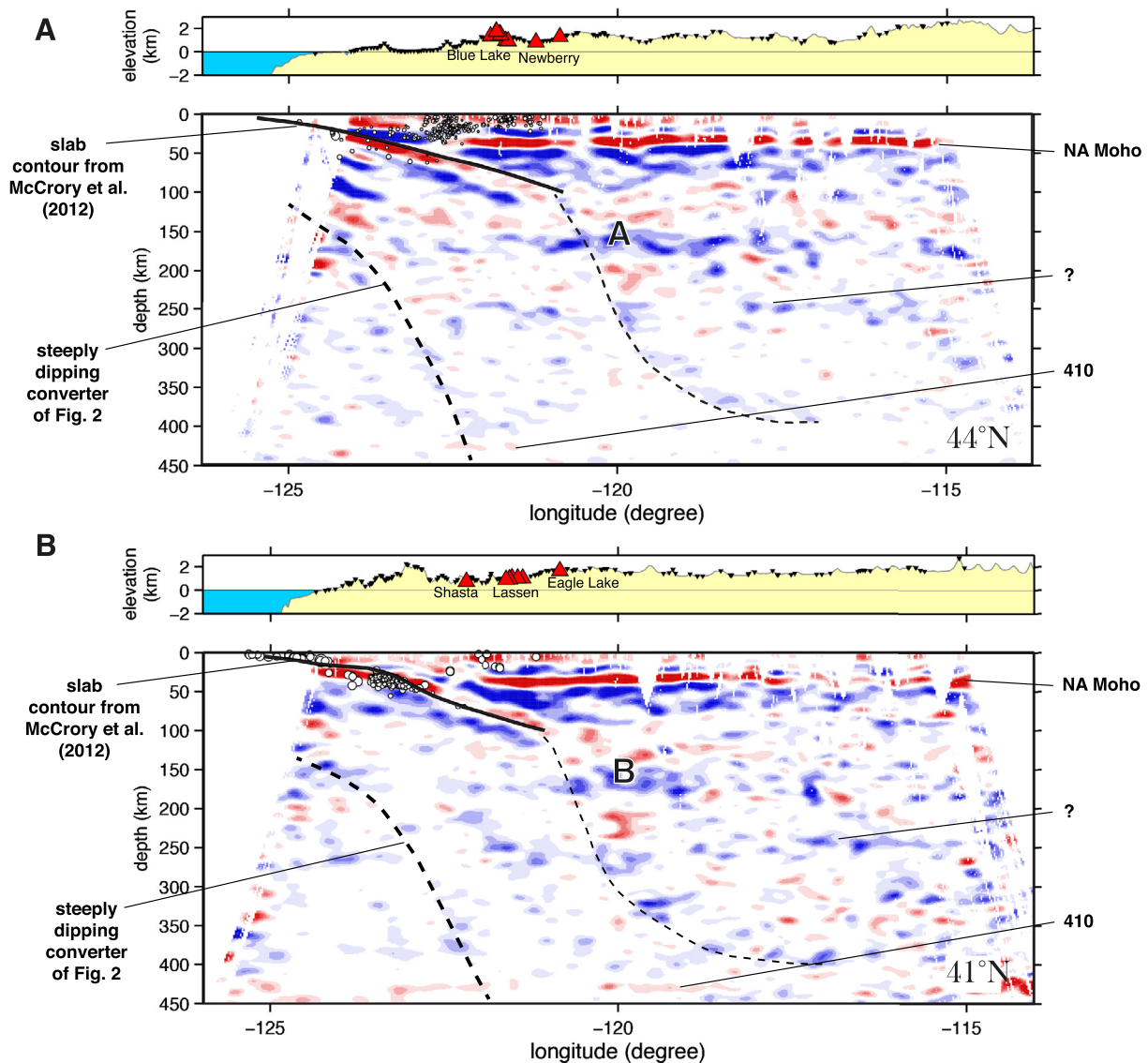


**Fig. 8.** Corrected reflectivity profiles of the Cascadia subduction zone. (A) At 44.25°N along the A–a profile across central Oregon. (B) At 41°N along the B–b profile across northern California. Red/blue areas show positive/negative amplitudes corresponding to increases/decreases of  $v_s$  respectively. The seismicity above and below the slab (McCrory et al., 2012) is indicated with open circles. The depth contour of the Gorda–Juan de Fuca plate from McCrory et al. (2012) is plotted with a black line. The dashed lines are inferred from reflectivity and seismic tomography (Fig. 4) and indicate the possible boundary delimiting the subducted plate from the mantle wedge. The thick black dashed line locates the steeply dipping signal of the multiples in Fig. 2. (For interpretation of the references to color in this figure legend, the reader is referred to the web version of this article.)

method is the identification of a  $\pi$  periodicity in the move-out of converted arrivals as a function of the back-azimuth (Levin and Park, 1997). A second method looks for different signatures of an interface on two versions of a CCP seismic image obtained from different back-azimuth sampling (Nábělek et al., 2009). We applied the second approach to our data but we couldn't isolate a clear anisotropic signal. Constraining anisotropy beneath Cascadia requires developing an approach able to separate the effect of anisotropy from the effect of dipping interfaces, which is clearly outside the scope of the present study. However, the similarity between our lithospheric interface and the one found by Audet (2013) in northern Cascadia suggests that his interpretation can reasonably be extrapolated to our observations for central Oregon and northern California. The negative converter that we observe thus could therefore represent the fossil fabric of the oceanic mantle.

At shallow depths, RF data and the tomographic model are in agreement (Fig. 9). The most reflective interfaces, i.e. the Moho of

the Gorda and Juan de Fuca plates, are off-centered from the fast slab anomalies. This offset is expected from the high frequency content of the RF data ( $>0.1$  Hz), largely insensitive to the broad velocity gradients (Bostock, 1999), but sensitive to the sharp  $v_s$  jump at the crustal compositional boundary atop the plate. We observe in RF data a change in the dip of the subduction near 100 km depth, from  $\sim 20^\circ$  to  $\sim 50^\circ$  (Fig. 8), which appears consistent with the steep slab imaged from tomography below northern California (Fig. 9).

Along both profiles, our RF images show little difference in the slab structure at all depths (Fig. 8). The signature of the Gorda and Juan de Fuca plates is faint beyond 200 km depth but intermittent signals seem to delimit the eastern edge of the slab (thin black dashed lines). We interpret these faint converters in the 100 km to 400 km depth range as pervasive reflectivity associated with deep slab-dehydration and metasomatism in the mantle wedge (Zheng et al., 2007) of the Cascadia subduction zone (Figs. 8–9). However, seismic tomography shows a continu-

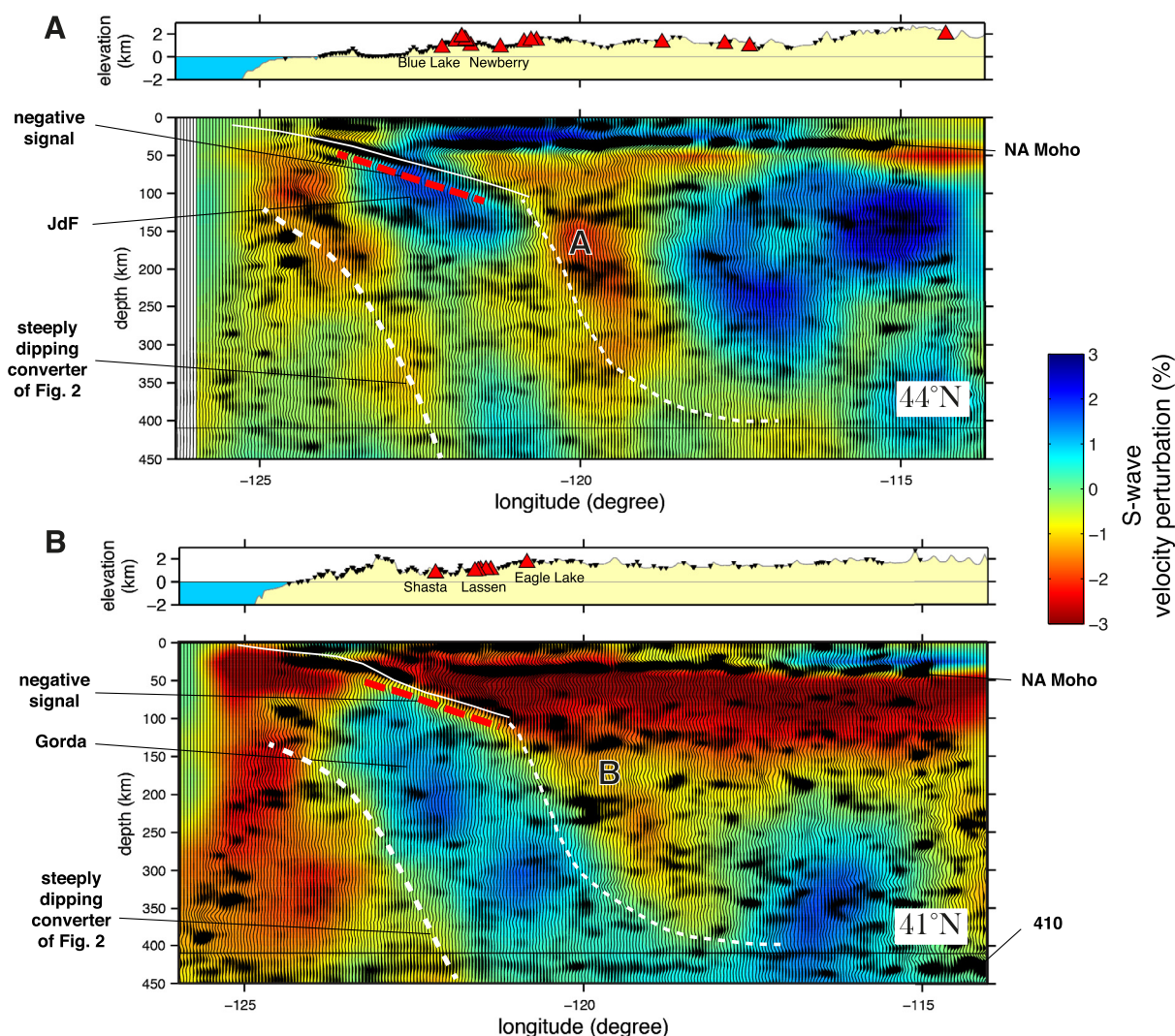


**Fig. 9.** Comparison with the seismic tomographic model DNA10 from Obrebski et al. (2011). Black wiggles correspond to the CCP stacked images from Fig. 2. The model in the background is DNA10, a regional shear-wave tomographic model from Obrebski et al. (2011). (A) Profile at 44.25°N along A–a in central Oregon. (B) Profile at 41°N along B–b in northern California. The plate contour from McCrory et al. (2012) is plotted with a white line. The thick red dashed line is the negative converter in the lithospheric oceanic mantle. The thin white dashed line indicates the possible boundary delimiting the subducted plate from the mantle wedge. The thick white dashed line locates the steeply dipping signal of the multiples in Fig. 2. (For interpretation of the references to color in this figure legend, the reader is referred to the web version of this article.)

ous slab structure down to at least 400 km depth below northern California (Fig. 9B), whereas in central Oregon the subduction seems to interrupt near 150 km depth (Fig. 9A). The slab gap in Oregon has been reported in many regional tomographic studies based on USArray data (e.g. Roth et al., 2008; Burdick et al., 2010; Obrebski et al., 2011). It is often explained by the absence of plate due to slab break-off (e.g. Obrebski et al., 2010), but Roth et al. (2008) proposed that it could also be a tomographic inversion artifact. The fact that despite the apparent slab gap in central Oregon (Fig. 9A), the deep converters exist also along the A–a profile (Fig. 8A), suggests that the subducted plate is present, although not detected in seismic tomography.

Near 160 km depth on both profiles, we find strong negative signals (labeled A and B in Fig. 8) in the continuation of the Gorda and Juan de Fuca plates. These A–B signals extend sub-horizontally toward the east. To our knowledge, this is the first observation of these seismic converters. Their locations coincide with larger scale low-velocity anomalies in tomography (e.g. Obrebski et al., 2011) (Fig. 9), and with conductive plumes imaged by magnetotelluric data (e.g. Meqbel et al., 2014). They could represent new observations of the sequence of dehydration and metasomatism in the

Cascadia subduction zone (Omori and Komabayashi, 2007). However, it is not clear how the negative signal labeled A can propagate through the slab (toward the west of the dashed line). Our synthetic tests for a flat stratification and a 20° dipping structure (Figs. 4 and 5) indicate that residual energy from the North American crustal multiples may remain in this depth range, so further investigation is required to confirm their origin.

#### 4. Conclusion

We used a multiple mode conversion imaging technique that efficiently remove artifacts from reverberated waves in layers above seismic interfaces, and allows imaging subduction structures. Compared to other techniques our approach is fast and computationally tractable on a desktop computer. We image the subduction of the Gorda and Juan de Fuca oceanic micro-plates below the North American continent. The interfaces between the subducting and overriding plates and the oceanic Moho are relocated at shallow depths (<120 km) with the correct dip angle (~20°). We report a pronounced negative converter from ~50 km to ~120 km depth, ~17 km below the dipping oceanic Mohos.

Its depth is consistent with fossil fabric generated at spreading ridges. We highlight faint converters in the mantle wedge above the subducted plates. Together with sub-horizontal seismic scatterers near 160 km depth, they could represent new observations of the sequence of dehydration and metasomatism in the Cascadia subduction zone.

## Acknowledgements

We thank the IRIS Data Management Center, the universities of Oregon, California, Berkeley, Rice, and the Earthscope program of the National Science Foundation for acquiring and providing the waveform data used in this study. This study was supported by a Chaire d'Excellence from CNRS. We thank two anonymous reviewers for the suggestions to improve the manuscript.

## References

- Abers, G.A., MacKenzie, L.S., Rondenay, S., Zhang, Z., Wech, A.G., Creager, K.C., 2009. Imaging the source region of Cascadia tremor and intermediate-depth earthquakes. *Geology* 37 (12), 1119–1122.
- Audet, P., 2013. Seismic anisotropy of subducting oceanic uppermost mantle from fossil spreading. *Geophys. Res. Lett.* 40 (1), 173–177.
- Audet, P., Bostock, M.G., Christensen, N.I., Peacock, S.M., 2009. Seismic evidence for overpressured subducted oceanic crust and megathrust fault sealing. *Nature* 457, 76–78. <http://dx.doi.org/10.1038/nature07650>.
- Audet, P., Bostock, M.G., Boyarko, D.C., Brudzinski, M.R., Allen, R.M., 2010. Slab morphology in the Cascadia fore arc and its relation to episodic tremor and slip. *J. Geophys. Res.* 115, 1–15.
- Beghein, C., Yuan, K., Schmerr, N., Xing, Z., 2014. Changes in seismic anisotropy shed light on the nature of the Gutenberg discontinuity. *Science* 343 (6176), 1237–1240.
- Bostock, M.G., 1999. Seismic waves converted from velocity gradient anomalies in the Earth's upper mantle. *Geophys. J. Int.* 138 (3), 747–756.
- Bostock, M.G., 2013. The Moho in subduction zones. *Tectonophysics* 609, 547–557.
- Bostock, M.G., Rondenay, S., 1999. Migration of scattered teleseismic body waves. *Geophys. J. Int.* 137 (3), 732–746.
- Bostock, M.G., Rondenay, S., Shragge, J., 2001. Multiparameter two-dimensional inversion of scattered teleseismic body waves 1. Theory for oblique incidence. *J. Geophys. Res.* Solid Earth 106 (B12), 30771–30782.
- Bostock, M.G., Hyndman, R.D., Rondenay, S., Peacock, S.M., 2002. An inverted continental Moho and serpentinization of the forearc mantle. *Nature* 417, 536–539.
- Burdick, S., van der Hilst, R.D., Vernon, F.L., Martynov, V., Cox, T., Eakins, J., Karasu, G.H., Tylell, J., Astiz, L., Pavlis, G.L., 2010. Model update January 2010: upper mantle heterogeneity beneath North America from traveltimes tomography with global and USArray transportable array data. *Seismol. Res. Lett.* 81 (5), 689–693.
- Cheng, C., Bodin, T., Allen, R.M., 2016. 3D pre-stack depth migration of receiver functions with the fast marching method: a Kirchhoff approach. *Geophys. J. Int.* <http://dx.doi.org/10.1093/gji/ggw062>.
- Debayle, E., Ricard, Y., 2012. A global shear velocity model of the upper mantle from fundamental and higher Rayleigh mode measurements. *J. Geophys. Res.* Solid Earth 117 (B10).
- Faccenda, M., 2014. Water in the slab: a trilogy. *Tectonophysics* 614, 1–30.
- Faccenda, M., Gerya, T.V., Burlini, L., 2009. Deep slab hydration induced by bending-related variations in tectonic pressure. *Nat. Geosci.* 2 (11), 790–793.
- Frederiksen, A.W., Bostock, M.G., 2000. Modelling teleseismic waves in dipping anisotropic structures. *Geophys. J. Int.* 141 (2), 401–412.
- Fuchs, K., Müller, G., 1971. Computation of synthetic seismograms with the reflectivity method and comparison with observations. *Geophys. J. Int.* 23 (4), 417–433.
- Grand, S.P., van der Hilst, R.D., 1997. Global seismic tomography: a snapshot of convection in the Earth. *GSA Today* 7, 1–7.
- Hacker, B.R., Peacock, S.M., Abers, G.A., Holloway, S.D., 2003. Subduction factory 2. Are intermediate-depth earthquakes in subducting slabs linked to metamorphic dehydration reactions? *J. Geophys. Res.* 108, 2030.
- Hetényi, G., 2007. Evolution of deformation of the Himalayan prism: from imaging to modelling. Doctoral dissertation. Université Paris Sud-Paris XI.
- Káráson, H., Van Der Hilst, R.D., 2000. Constraints on mantle convection from seismic tomography. In: Richards, M.A., Gordon, R.G., Van Der Hilst, R.D. (Eds.), *The History and Dynamics of Global Plate Motions*. American Geophysical Union, Washington D.C.
- Kennett, B.L.N., Engdahl, E.R., 1991. Traveltimes for global earthquake location and phase identification. *Geophys. J. Int.* 105 (2), 429–465.
- Kim, Y., Miller, M.S., Pearce, F., Clayton, R.W., 2012. Seismic imaging of the Cocos plate subduction zone system in central Mexico. *Geochem. Geophys. Geosyst.* 13 (7).
- Langston, C.A., 1979. Structure under Mount Rainier, Washington, inferred from teleseismic body waves. *J. Geophys. Res.* 84 (B9), 4749–4762.
- Levin, V., Park, J., 1997. Crustal anisotropy in the Ural Mountains foredeep from teleseismic receiver functions. *Geophys. Res. Lett.* 24 (11), 1283–1286.
- Ligorria, J.P., Ammon, C.J., 1999. Iterative deconvolution and receiver-function estimation. *Bull. Seismol. Soc. Am.* 89 (5), 1395–1400.
- Liu, K., Levander, A., Zhai, Y., Porritt, R.W., Allen, R.M., 2012. Asthenospheric flow and lithospheric evolution near the Mendocino Triple Junction. *Earth Planet. Sci. Lett.* 323, 60–71.
- Lucente, F.P., Piana Agostinetti, N., Moro, M., Selvaggi, G., Di Bona, M., 2005. Possible fault plane in a seismic gap area of the southern Apennines (Italy) revealed by receiver function analysis. *J. Geophys. Res.* Solid Earth 110 (B4).
- MacKenzie, L.S., Abers, G.A., Rondenay, S., Fischer, K.M., 2010. Imaging a steeply dipping subducting slab in Southern Central America. *Earth Planet. Sci. Lett.* 296 (3), 459–468.
- McCrory, P.A., Blair, J.L., Waldhauser, F., Oppenheimer, D.H., 2012. Juan de Fuca slab geometry and its relation to Wadati–Benioff zone seismicity. *J. Geophys. Res.* 117, B09306.
- Meqbel, N.M., Egbert, G.D., Wannamaker, P.E., Kelbert, A., Schultz, A., 2014. Deep electrical resistivity structure of the northwestern US derived from 3-D inversion of USArray magnetotelluric data. *Earth Planet. Sci. Lett.* 402, 290–304.
- Nábělek, J., Hetényi, G., Vergne, J., Sapkota, S., Kafle, B., Jiang, M., Su, H., Chen, J., Huang, B.S., 2009. Underplating in the Himalaya–Tibet collision zone revealed by the Hi-CLIMB experiment. *Science* 325 (5946), 1371–1374.
- Nedimović, M.R., Bohnenstiehl, D.R., Carbotte, S.M., Canales, J.P., Dziak, R.P., 2009. Faulting and hydration of the Juan de Fuca plate system. *Earth Planet. Sci. Lett.* 284 (1), 94–102.
- Obrebski, M., Allen, R.M., Xue, M., Hung, S.H., 2010. Slab–plume interaction beneath the Pacific Northwest. *Geophys. Res. Lett.* 37 (14).
- Obrebski, M., Allen, R.M., Pollitz, F., Hung, S.H., 2011. Lithosphere–asthenosphere interaction beneath the western United States from the joint inversion of body-wave traveltimes and surface-wave phase velocities. *Geophys. J. Int.* 185, 1003–1021.
- Omori, S., Komabayashi, T., 2007. Subduction zone: the water channel to the mantle. In: Yuen, D.A., et al. (Eds.), *Superplumes: Beyond Plate Tectonics*. Springer, Netherlands, pp. 113–138.
- Reynard, B., Nakajima, J., Kawakatsu, H., 2010. Earthquakes and plastic deformation of anhydrous slab mantle in double Wadati–Benioff zones. *Geophys. Res. Lett.* 37 (24).
- Rondenay, S., 2009. Upper mantle imaging with array recordings of converted and scattered teleseismic waves. *Surv. Geophys.* 30 (4–5), 377–405.
- Rondenay, S., Abers, G.A., Van Keken, P.E., 2008. Seismic imaging of subduction zone metamorphism. *Geology* 36 (4), 275–278.
- Roth, J.B., Fouch, M.J., James, D.E., Carlson, R.W., 2008. Three-dimensional seismic velocity structure of the northwestern United States. *Geophys. Res. Lett.* 35 (15).
- Schmandt, B., Dueker, K.G., Hansen, S.M., Jasinsek, J.J., Zhang, Z., 2011. A sporadic low-velocity layer atop the western US mantle transition zone and short-wavelength variations in transition zone discontinuities. *Geochem. Geophys. Geosyst.* 12, 1–26.
- Schimmel, M., Paulssen, H., 1997. Noise reduction and detection of weak, coherent signals through phase-weighted stacks. *Geophys. J. Int.* 130 (2), 497–505.
- Shinohara, M., Fukano, T., Kanazawa, T., Araki, E., Suyehiro, K., Mochizuki, M., Nakahigashi, K., Yamada, T., Mochizuki, K., 2008. Upper mantle and crustal seismic structure beneath the Northwestern Pacific Basin using a seafloor borehole broadband seismometer and ocean bottom seismometers. *Phys. Earth Planet. Inter.* 170 (1), 95–106.
- Song, T.R.A., Kim, Y., 2012. Anisotropic uppermost mantle in young subducted slab underplating Central Mexico. *Nat. Geosci.* 5 (1), 55–59.
- Song, T.R.A., Helmberger, D.V., Grand, S.P., 2004. Low-velocity zone atop the 410-km seismic discontinuity in the northwestern United States. *Nature* 427 (6974), 530–533.
- Suckale, J., Rondenay, S., Sachpazi, M., Charalampakis, M., Hosa, A., Royden, L.H., 2009. High-resolution seismic imaging of the western Hellenic subduction zone using teleseismic scattered waves. *Geophys. J. Int.* 178 (2), 775–791.
- Tauzin, B., Debayle, E., Wittlinger, G., 2010. Seismic evidence for a global low-velocity layer within the Earth's upper mantle. *Nat. Geosci.* 3 (10), 718–721.
- Tauzin, B., Van Der Hilst, R.D., Wittlinger, G., Ricard, Y., 2013. Multiple transition zone seismic discontinuities and low velocity layers below western United States. *J. Geophys. Res.* Solid Earth 118 (5), 2307–2322.
- Walowski, K.J., Wallace, P.J., Hauri, E.H., Wada, I., Clynne, M.A., 2015. Slab melting beneath the Cascade Arc driven by dehydration of altered oceanic peridotite. *Nat. Geosci.* 8 (5), 404–408.
- Wittlinger, G., Farra, V., Vergne, J., 2004. Lithospheric and upper mantle stratifications beneath Tibet: new insights from Sp conversions. *Geophys. Res. Lett.* 31 (19).
- Xue, M., Allen, R.M., 2007. The fate of the Juan de Fuca plate: implications for a Yellowstone plume head. *Earth Planet. Sci. Lett.* 264, 266–276.
- Zheng, Y., Lay, T., Flanagan, M.P., Williams, Q., 2007. Pervasive seismic wave reflectivity and metasomatism of the Tonga mantle wedge. *Science* 316, 855–859.